

Performance of universal machine learning potentials in global optimization

Edan T. Marcial, Laxman Chaudhary, Olesya Gorbunova, and Aleksey N. Kolmogorov*

*Department of Physics, Applied Physics, and Astronomy,
Binghamton University-SUNY, Binghamton, New York 13902, USA*

(Dated: March 2, 2026)

Rapid development of universal machine learning potentials (uMLPs) and expansion of training data sets are reshaping the state of the art in atomistic simulation, highlighting the need for concurrent systematic benchmarking of their capabilities. Global optimization is among the most demanding uMLP applications because unconstrained exploration includes probing motifs not present in reference sets. We examined the latest generation of uMLPs in unconstrained evolutionary searches to assess whether these models can consistently predict complex crystal structure ground states across diverse inorganic systems. Our findings demonstrate that the considered M3GNet, MACE, SevenNet, EquiformerV2, MatterSim, GRACE, eSEN, Orb-v3, and PET-MAD models span a wide performance range, from near *ab initio* to essentially non-predictive, in their ability to resolve competing phases within low-energy basins. Additional tests on hcp-Zn, MB₄ (M = Cr, Mn, and Fe), and LiB_y ($y \approx 0.9$) ground states reveal that several uMLPs capture fine energy differences arising from subtle electronic structure features.

I. INTRODUCTION

Machine learning interatomic potentials (MLPs) have earned a place in mainstream computational materials research as efficient alternatives to electronic structure calculations. The first models capable of describing arbitrary atomic environments, the Behler–Parrinello neural networks (NN) and the Gaussian approximation potentials (GAPs), demonstrated that density functional theory (DFT)-level accuracy can be retained in simulations where system sizes and times scales are extended by orders of magnitude [1, 2]. In the following years, MLPs were applied to a broad range of tasks, including molecular dynamics simulations of phase stability, thermal transport, and mechanical response, geometry optimizations of clusters, surfaces, and extended defects, and transition state searches of diffusion and reaction pathways [3–5].

The impact of MLPs on crystal structure prediction was less immediate. Many early studies focused on elemental materials, *e.g.*, B, C, Si, and P, and either reproduced known ground states or identified metastable polymorphs [6–9]. The first examples of new thermodynamically stable compounds found with MLP-accelerated global searches appeared only in the late 2010s [10–14]. The main challenge was the construction of practical potentials that could resolve small energy differences between competing structures while remaining reliable in previously unexplored regions of configuration space. This was addressed, in particular, by extending models from elements to multicomponent systems and by introducing automated workflows for iterative reference data generation and model parametrization [15–18]. The resulting MLPs offered genuine acceleration, leading to the identification of new complex M-Sn [11, 12] and SiH₄ [19] ground states overlooked in prior searches at the DFT

level. Despite these successes, the need to build robust system-specific models has limited the widespread use of MLPs in routine crystal structure prediction.

Recently introduced universal MLPs (uMLPs) represent a conceptually different approach. Trained on large and broadly representative materials databases, these models enable users to either bypass system-specific parametrization altogether or carry out further fine-tuning for target applications. uMLPs have already been used for large-scale screening of stability, transport properties, and finite-temperature behavior and have been benchmarked in several studies [20–30]. In particular, Yu *et al.* [23] assessed four uMLPs on equation-of-state curves, relaxed geometries, and formation energies for extensive sets of crystalline materials. Riebesell *et al.* [25] developed the Matbench Discovery framework to evaluate property predictions, such as relaxed formation energies and distances to the convex hull, from unrelaxed structures. Chiang *et al.* [26] presented the MLIP Arena system, which compares the performance of nine uMLPs across equation-of-state curves and molecular dynamics simulations, focusing on physically grounded performance independent of DFT references. Tahmasbi *et al.* [27] extended these evaluations to global structure searches by using a minima hopping algorithm to probe the potential energy surfaces of unary materials. These studies establish that current uMLPs are sufficiently accurate for local optimization of pre-defined structure prototypes and near-equilibrium properties as well as applicable to global optimization of elemental systems, but their performance in unconstrained structure searches for stable chemically diverse inorganic compounds has yet to be explored systematically.

In this work, we assess the performance of the latest generation of uMLPs in global structure searches in multicomponent systems. The workflow complements existing benchmarks by probing the surrogate potential energy surfaces beyond the configurations represented in the training datasets, as we investigated materials with

* kolmogorov@binghamton.edu

TABLE I. Overview of uMLPs evaluated in this work, with additional information given in Section II B. For each model we report the publication year, model architecture, featurizing basis functions, training data source, reference DFT method, training set size, and the parameter count. SBF, GK, and RBF stand for spherical Bessel functions, Gaussian kernels, and radial basis functions, respectively. Blank entries represent data not reported or readily available.

uMLP version	ID adopted	Year reported	uMLP architecture	Featurizing basis functions	Dataset sources	DFT functional	Structures ($\times 10^6$)	Parameters ($\times 10^6$)
M3GNet	MG	2022	GNN	Bessel RBF Y_ℓ^m	MP	PBE	0.2	1.1
MACE	MC	2023	Equiv. MPNN	Bessel RBF Y_ℓ^m	MATPES-PBE	PBE		19.8
SevenNet-MF	SN	2024	E(3) NequIP	Bessel RBF Y_ℓ^m	OMat24 MPtrj sAlex	PBE	113	25.7
EquiformerV2	EQ	2024	E(3)/SE(3)	Bessel RBF Y_ℓ^m	OMat24 MPtrj sAlex	PBE	102	98.4
MatterSim	MS	2024	M3GNet Graph	SBF Y_ℓ^m GK	MatterSim	PBE	17	4.6
GRACE-2L	GR	2025	ACE Graph	Chebyshev RBF Y_ℓ^m	OMat24	PBE		25.2
eSEN	EN	2025	E(3)/SE(3)	Polynomial EF RBF	OMat24	PBE	10	30.2
Orb-v3	OR	2025	GNS	Bessel RBF Y_ℓ^m	OMat24	PBE	55	25.5
PET-MAD	PT	2025	GNN	Machine learned	MAD	PBEsol	0.1	3.5

both well-established [31–40] and recently proposed [11, 12, 41] ambient-pressure ground states. The nine selected models, M3GNet [20], MACE [42, 43], SevenNet [44, 45], EquiformerV2 [46–49], MatterSim [50], GRACE [51, 52], eSEN [47, 53], Orb-v3 [54, 55], and PET-MAD [56], span various architectures and vastly different training sets, but nearly all of them were fitted to the same DFT approximation (see Table I). To determine their suitability for ground state searches across materials with different chemistries and bonding types, we used the uMLPs as out-of-the-box surrogate models combined with an evolutionary algorithm [16]. Within this framework, which previously enabled the prediction of new thermodynamically stable compounds [11, 12], the small pools of identified low-energy candidate structures are re-examined with the reference DFT approximation. We also consider three challenging cases, hcp-Zn with an anomalous c/a ratio, distorted MB_4 derivatives ($M = \text{Cr, Mn, and Fe}$), and off-stoichiometric LiB_y phases, in which electronic features are known to play a key role in defining the ground state structure. By comparing the uMLPs against not only the Perdew–Burke–Ernzerhof (PBE) [57] but also the widely used PBE generalized gradient approximation for solids (PBEsol) [58] and regularized-restored strongly constrained and appropriately normed ($r^2\text{SCAN}$) [59] exchange-correlation functionals, we demonstrate that some models, most notably eSEN, reproduce the reference method with accuracy better than the systematic spread among these DFT approximations.

II. METHODOLOGY

A. DFT Calculations

All DFT calculations were performed with the Vienna *ab initio* simulation package (VASP) [60–63] and projector-augmented wave potentials [64] with the maximum number of semi-core electrons for each ele-

ment. We used a 500 eV plane-wave cutoff and dense Monkhorst–Pack [65] k-meshes with $\Delta k \leq 2\pi \times 0.025 \text{ \AA}^{-1}$ to ensure good numerical convergence. All final energies were evaluated with the tetrahedron integration method with Blöchl corrections [66] for fully optimized unit cells. As the default DFT method, we employed the PBE exchange-correlation functional [57] within the generalized gradient approximation (GGA) [67]. For examining systematic DFT errors, we also carried out calculations with the PBEsol [58] functional, the $r^2\text{SCAN}$ functional [59] that is currently adopted in the Materials Project [68] for its improved description of materials formation energies, and four different parametrizations [69–72] that treat van der Waals (vdW) interactions important in layered materials. The full structural information for relevant phases is provided in the Supplemental Material (Listings 1-32).

B. uMLPs

Pretrained models were taken directly from publicly available repositories and were not fine-tuned in this study in order to evaluate their baseline performance. M3GNet (denoted as MG henceforth) is a pioneering model trained on three-body interactions across 89 elements [20]. MACE (MC) utilizes the atomic cluster expansion as a descriptor and performs efficient calculations due to its streamlined message-passing architecture [42, 43]. SevenNet (SN) maintains equivariance, incorporates the architecture of NequIP [73], and uses a combination of low- and high-fidelity data in its training [44, 45]. EquiformerV2 (EQ) is an equivariant model that builds on eSCN convolutions [74] for higher degree representations of atomic environments [46–49]. MatterSim (MS, version MatterSim-v1.0.0–5M) uses active learning, uncertainty-aware data sampling, and a training dataset containing off-equilibrium structures under a variety of temperatures and pressures [50]. GRACE (GR) uses equivariant message passing and extends the

atomic cluster expansion to recursively evaluated star- and tree-like basis functions, constructing a complete basis for describing atomic interactions [51, 52]. eSEN (EN) is a message-passing NN with an Equiformer-like architecture [46] designed to strictly maintain equivariance and a smoothly varying potential energy surface [47, 53]. The conservative Orb-v3 (OR) variant is a roto-equivariant graph network simulator (GNS) that builds off of the previous generation of direct-force Orb models [54, 55]. The recently introduced PET-MAD (PT, version `pet-mad-v1.0.2`) is a rotationally unconstrained, transformer-based model trained on the Massive Atomic Diversity (MAD) dataset [56]. Among these uMLPs, EQ is the only explicitly non-conservative model that calculates forces directly rather than as an energy gradient. Information on uMLP relative efficiencies can be found in previous studies, *e.g.*, Ref. [56]. In the present tests, local structure relaxations were performed with MatGL [75] in MG simulations or with the Atomic Simulation Environment (ASE) for all other uMLPs [76], and the accuracy of each uMLP’s predictions was evaluated against the DFT functional used in its training, *i.e.*, PBEsol for PET-MAD and PBE for the rest (see Table I). Importantly, none of the tested properties involved absolute DFT energies, which made results independent of the atomic reference values in pseudopotentials, particularly relevant in the case of the PT baseline method [56].

C. Global search benchmarking protocol

Efficient acceleration of *ab initio* global structure optimization depends on surrogate models meeting two key requirements [11, 16, 27, 77]. First, a uMLP must be robust enough that the PES is not dominated by spuriously overstabilized unphysical structures and that the true DFT ground state can be reached from a uMLP minimum structure via a barrierless trajectory. Second, it must be sufficiently accurate that the uMLP-based energy ranking retains, within a tractably small pool, at least one candidate that converges to the true ground state upon DFT re-optimization. Systematic comparison of the uMLPs’ performance is not straightforward due to the inherently stochastic nature of global optimization methods. The suitability of uMLPs for finding ground states with no structural input was benchmarked with the following protocol.

The starting point involved carrying out typical zero-temperature fixed-composition evolutionary searches appropriate for locating medium-sized ground states of crystalline solids [11, 12]. Populations of 100 structures with a given number of atoms were seeded randomly and evolved over 100 generations with standard operations implemented in the module for *ab initio* structure evolution (MAISE) [16]; mutation of individual members (20%), crossover of two parent structures (60%), and injection of additional random seeds (20%). Local optimizations with a uMLP proceeded until the maximum

atomic force fell below $0.05 \text{ eV}/\text{\AA}$, which was sufficient for detecting and eliminating duplicates based on the similarity in energy and structural fingerprint [16, 78]. To remove any underconverged duplicates, all visited minima up to 20 meV/atom above the best candidate and with the similarity fingerprint scalar product below 0.92, controlled by the SCUT flag in MAISE, were optimized with the uMLP with a finer $0.001 \text{ eV}/\text{\AA}$ tolerance and filtered again with the 0.92 threshold. For compounds where few minima were found after filtering, we increased the energy window by 10 meV/atom and repeated the filtering step until more than 10 minima were found or the energy window reached 100 meV/atom (*e.g.*, for LiB_3). Inspection of the pools provided information on the quality of the PES fit for individual uMLPs, judged by the presence of minima significantly below the global one and an overabundance of low-symmetry satellite minima around structures improperly modeled as dynamically unstable. In the latter case, we used a more restrictive 0.82 SCUT flag for our selection criterion.

The variance in the number of candidate structures per uMLP pool complicated consistent quantitative assessment of the models’ ability to select competitive candidates in relevant regions of the configuration space. To account for the non-deterministic sampling of low-energy basins and ensure that each uMLP test pool included the ground state, we merged all minima found with uMLPs that offered a meaningful description of the particular compound into a single pool. Subsequent relaxation ($0.001 \text{ eV}/\text{\AA}$ tolerance) and filtering (0.92 SCUT) of the aggregate generated comparable pools for each classical model. Finally, structures in each uMLP pool were re-optimized with the reference DFT method. The fingerprint scalar product and the DFT energy difference between the uMLP- and DFT-relaxed configurations, defining structure and energy proximity metrics, respectively, indicated how close the competing minima were on the surrogate and reference PESs. The ranking accuracy was gauged using an RMSE defined as

$$\text{Ranking RMSE} = \left[\frac{\sum_{n=1}^N (E_n^{\text{uMLP}} - E_n^{\text{DFT}} - \Delta\bar{E})^2}{N - 1} \right]^{\frac{1}{2}}.$$

Here, N is the number of structures in each pool, $\Delta\bar{E} = \bar{E}^{\text{uMLP}} - \bar{E}^{\text{DFT}}$ is the difference between pool averages, and the $N - 1$ factor accounts for the Bessel correction. This metric differs from the typically reported overall model error in that it eliminates the average shifts irrelevant to relative stability, evaluates energies of configurations fully relaxed within their respective methods rather than identical snapshots, and probes accuracy only in the low-energy basins important in global structure searches.

III. EVOLUTIONARY OPTIMIZATION

Evolutionary searches were performed for 12 inorganic nonmagnetic compounds listed in Table II with

TABLE II. uMLP energy difference of best candidates from evolutionary searches relative to reference ground states given in meV/atom. The relative rank of reference structures found in each pool is given as a positive superscript. Searches where the global minimum was not found have a positive energy difference or a zero superscript.

uMLP ID	LiB ₃ tP16	Be ₄ B tP10	TiO ₂ mS24	MgIr ₂ hP12	Pd ₅ Sn ₃ mS32	Li ₃ Sn hR48	MgB ₃ C ₃ oI28	Na ₂ CN ₂ mS10	CYI mS12	Na ₂ IrO ₃ mS24	Si ₃ CaPt tI10	AgClO ₄ tI12
EN	0.0	0.0	0.0	0.0	0.0	0.0	0.0	0.0 ²	0.0	0.0	0.0	-187.4 ⁰
EQ	0.0	0.0	0.0	0.0	0.0	0.0	22.3	1.4	0.0	0.0	0.0	-185.3 ⁰
OR	0.0	0.0	0.0	0.0	0.0	0.0	52.3	-1.6 ²	0.0	0.0	0.0	-189.9 ⁰
SN	0.0	0.0	0.0	0.0	0.0	0.0	0.0	-3.4 ⁴	0.0	0.0	0.0	-205.7 ⁰
GR	0.0	0.0	-3.4 ²	0.0	0.0	-2.6 ⁴	0.0	0.0	0.0	0.0	0.0	-210.9 ⁰
MC	0.0	0.0	-37.0 ²⁷	0.0	0.0	-7.2 ²	-45.1 ⁰	-26.1 ⁵	0.0	0.0	-15.8 ⁵	-1e4 ⁰
MS	14.8	0.0	0.0	0.0	0.0	0.0	-17.6 ⁰	-15.0 ⁰	0.0	0.0	0.0	-179.0 ⁰
PT	0.0	0.0	-5.2 ²	0.0	0.0	0.0	20.4	0.0	0.0	0.0	0.0	-157.0 ⁰
MG	-47.6 ⁰	-14.5 ⁰	-9.4 ⁰	-29.7 ⁰	-3.7 ⁰	-14.9 ⁰	-180.3 ⁰	0.0	-58.9 ¹	0.0	-14.8 ⁰	-220.8 ⁰

bonding environments ranging from extended metal-stabilized covalent-ionic frameworks to interpenetrating metal-metalloid sublattices and structural complexities ranging from 5 to 16 atoms per primitive unit cell (see Table S1). The inclusion of Li₃Sn, Pd₅Sn₃, and MgB₃C₃ with recently proposed prototypes [11, 12, 41] served to probe whether the uMLPs can recognize unfamiliar, non-sampled motifs as ground states.

Table II summarizes the qualitative outcome of the searches. For each model and compound, we report the uMLP energy of the corresponding lowest-energy candidate relative to the ground state of the reference DFT method and the position of the DFT ground-state structure within the uMLP-ranked pool as a superscript. A run was counted as successful whenever the DFT ground state appeared within the low-energy shortlist, even if it was not ranked first by the uMLP. We emphasize that the table is not intended as a high-confidence scorecard. Although the total number of uMLP local optimizations exceeded two million, this dataset is not statistically sufficient to disentangle whether missed ground states reflect surrogate deficiencies or seed/trajectory dependence in the evolutionary exploration. To mitigate the latter, we repeated failed runs up to three times with different random seeds and, for the particularly challenging MgB₃C₃ case, employed a TETRIS-based generation [79] of initial structures containing B-C building blocks, which substantially improved convergence but did not guarantee success.

Evolutionary searches with nearly all uMLPs easily reached global minima for the majority of considered compounds, mostly independent of the primitive unit cell size or perceived complexity. For example, the relatively large LiB₃ ground state (tP16) is comprised of compact B₆ units that recur frequently across metal boride chemistries [80], which is apparently well reproduced as a broad basin of attraction on surrogate PESs. Likewise, the low-symmetry Na₂IrO₃ (mS24) features a typical layered arrangement of edge-sharing IrO₆ octahedra, which tends to constrain the accessible low-energy motifs. The recently proposed Li₃Sn (hR48) and Pd₅Sn₃ (mS32) ground states with new structure types turned out not to pose particular difficulty, as their local environments

can be viewed as ordered decorations of familiar metallic and metal-metalloid coordination motifs [11, 12], and the uMLPs learned the underlying stability trend well enough to identify these phases as global minima.

The few misses, either failing to access the global-minimum basin or misranking closely competing minima, were concentrated in systems that are challenging even at the DFT level. TiO₂ exhibits a rich polymorphism, with the relative stability of low-energy phases being highly sensitive to the treatment of dispersive and correlation effects [40]. This complexity of the PES helps frame why two uMLPs reversed the stability order of anatase (tI12) and the PBE-level ground state bronze (mS24) and why another did not allow the searches to log the ground state as a viable candidate. The uMLP-based exploration successfully recovered other known phases, namely, rutile (tP6), columbite (oP12), and baddeleyite (mP12), which indicates that the models correctly distinguished the PBE ground state from a realistic line-up of candidates. CYI (mS12) features Y₂I₂ layers with embedded C₂ dimers and requires a careful treatment of the vdW bonding. Most considered uMLPs struggled to resolve the favorability of alternative stackings due to a 1–2 Å overestimation of the interlayer spacing, an artifact inherited from the underlying semi-local DFT approximations that miscalculated the measured values by 0.2–0.5 Å. Global optimization of AgClO₄ with all nine uMLPs produced numerous spuriously deep minima containing O₂ dimers, such as mS24 given in the Supplemental Material (Fig. S1), starkly contrasting the accepted tI12 ground state built from ClO₄ tetrahedra. This pathology indicates that the considered uMLPs are not sufficiently familiar with molecular oxygen to disfavor its appearance in solid-state phases, which should be straightforward to fix by retraining the models on datasets that include this motif.

Beyond the primary intended benchmarking objective, our global searches with several uMLPs unexpectedly uncovered two phases more stable at their reference DFT level than the previously reported ground states. For Na₂CN₂, a substantially less dense packing of CN₂ units in a tI10 candidate (17.8 Å³/atom) than in the known mS10 structure (13.4 Å³/atom) improved the PBE-level

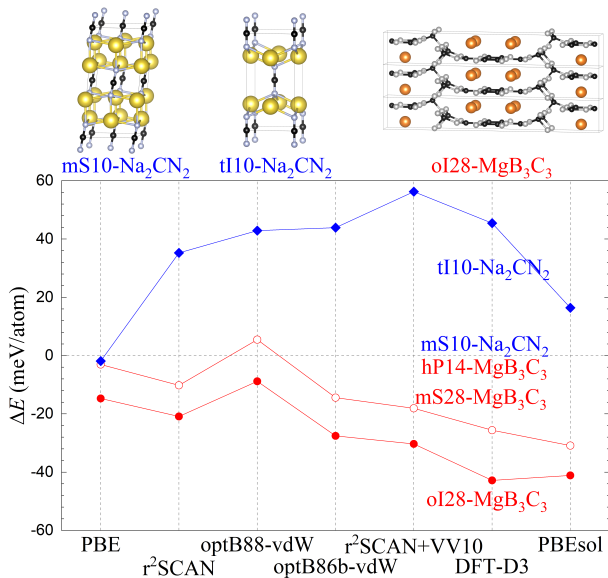


FIG. 1. Stability of the tI10-Na₂CN₂, mS28-MgB₃C₃, and ol28-MgB₃C₃ phases identified in this work relative to reported mS10-Na₂CN₂ and hP14-MgB₃C₃ evaluated with common DFT functionals.

stability by 1.9 meV/atom (see Fig. 1). However, all other tested functionals soundly disfavor tI10 relative to mS10 by 16-56 meV/atom, which makes the outlier a likely PBE-specific artifact. For MgB₃C₃, proposed to be a high- T_c superconductor in hP7 [81] or hP14 [41] honeycomb layer structures potentially accessible through deintercalation of the known MgB₂C₂ compound, prior *ab initio* searches located an mS28 phase with an alternative layered morphology considered more stable by a set of DFT functionals [41]. The current uMLP-accelerated global optimization generated an ol28 polymorph, shown in Fig. 1, with a BC framework connected in 3D via sp³ links uniformly favored by all tested DFT approximations.

The quantitative correspondence between surrogate and DFT low-energy landscapes was assessed by creating merged pools of minima located in all uMLP searches and using the three metrics described in Section II C. Table S1 shows a relatively large dispersion in the number of candidate phases in each uMLP’s evolutionary run pool, *e.g.*, between 14 for MC and 46 for PT for Li₃Sn, which illustrates why aggregating relevant minima was necessary for evaluating the uMLP performance on a more comparable basis. After joining all individual uMLP pools, with the exception of unreasonably large MG sets (see Table S1), we reoptimized the structures with each uMLP and removed duplicates. To enable a controlled comparison of alternative DFT flavors and the MG model, we chose the representative EN set. The resulting test sets for 11 compounds (not including AgClO₄) were mostly comparable in size, varying between 440 and 750 structures, with only one pool (EQ) exceeding 2,000 structures (Table S1), and were sufficiently large for the metric averages

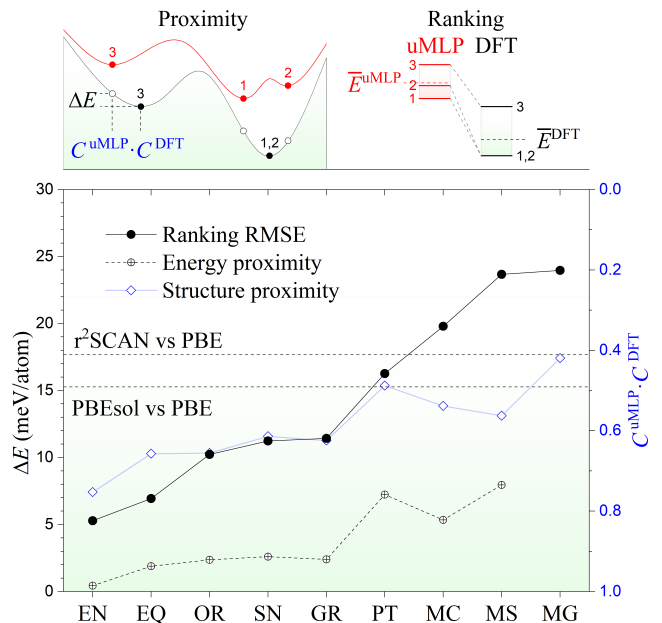


FIG. 2. Performance metrics on merged pools assessed relative to the reference DFT method, PBEsol for PT and PBE for the rest, and averaged over 11 compounds, excluding AgClO₄. The schematics at the top clarify the definitions of the proximity and ranking metrics introduced in the text. The representative merged EN pools were used to evaluate the metrics for the alternative DFT approximations and MG, with dashed horizontal lines marking the ranking RMSE for PBEsol and r²SCAN relative to PBE. The energy proximity average for MG exceeded 70 meV/atom (see Fig. S2 for further discussion).

to be statistically significant. In particular, we found the metric values to be close when computed as simple or size-weighted (as $N_{\text{compound}}^{\text{minima}}/N_{\text{total}}^{\text{minima}}$) averages across the considered compounds.

Fig. 2 summarizes the pool size-weighted metrics measuring the proximity of uMLP minima to the corresponding DFT counterparts and ranking fidelity within a low-energy shortlist. The changes in the RDF fingerprint and the DFT energy upon re-optimization span 0.42–0.75 and 1–8 meV/atom, respectively, with EN showing particularly small deviations. The fact that the average DFT relaxation produces only a modest and fairly systematic energy drop is important for downstream selection strategies that aim to improve effective ranking. For instance, our study on Au clusters [77] showed that a hybrid workflow, in which structures are relaxed with a NN potential while final energies are evaluated with single-shot DFT, can markedly improve convergence to the ground state, and that the added DFT cost during the evolutionary run can be offset by the reduction in pool sizes.

Some of the ranking RMSEs, ranging between 5 and 24 meV/atom, are notably lower than the overall errors typically reported for uMLPs, *e.g.*, around 20 meV/atom in MatBench tests [25]. This observation is consistent

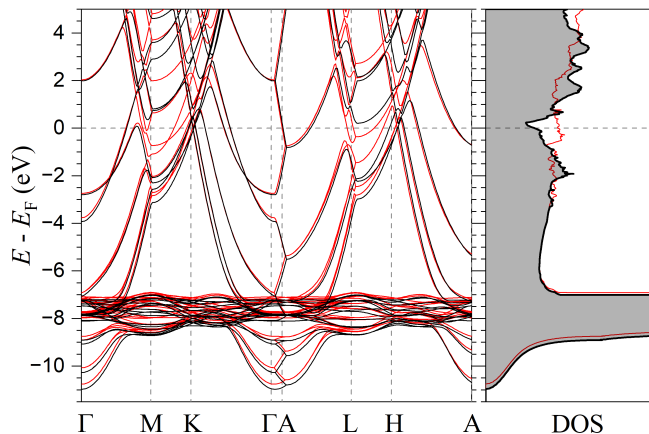


FIG. 3. Band structure and density of states calculated with DFT-PBE for hcp-Zn (black) and fcc-Zn (red) represented with 6-atom hexagonal unit cells at the experimental $c/a = 1.826$ ratio.

with the different functional purpose of this metric that involves only competing structures near the ground states and explicitly removes the average energy shift between uMLP and DFT pools. Fig. S2 breaks down the ranking RMSE by compound and shows that the values are reasonably consistent across distinct chemical classes. The violin plots presented in Fig. S3 underscore a general absence of outliers that could dominate and skew the computed RMSEs. The results show that relative energy accuracy correlates with the uMLP fitted-parameter count listed in Table I. Two models outperforming this trend are the medium-tier EN that slightly surpasses the largest-sized EQ and the small-tier PT that approaches the level of the medium-sized uMLPs.

Finally, it is instructive to compare the uMLPs against our system-specific Behler-Parrinello NN potentials fitted in previous studies for two M-Sn binaries [11, 12], with the reported total RMSE and the current ranking RMSEs of 10.2 meV/atom and 10.1 meV/atom for Li-Sn, and 9.6 meV/atom and 14.9 meV/atom for Pd-Sn, respectively. Nearly all uMLPs fare better, highlighting the benefit of training larger architectures with more flexible descriptors on more extensive datasets across the periodic table, which captures transferable stability trends across both structures and chemistries.

IV. GROUND STATE PERTURBATIONS

A. Ground state of Zn

Among hcp metals, Zn is known to exhibit a c/a ratio significantly deviating from the ideal close-packed $\sqrt{8/3} \approx 1.633$ value, an anomalous geometry attributed to the underlying electronic structure [82–84]. Häussermann and Simak [82] argued that the axial anisotropy is driven by a band-energy gain due to an s –

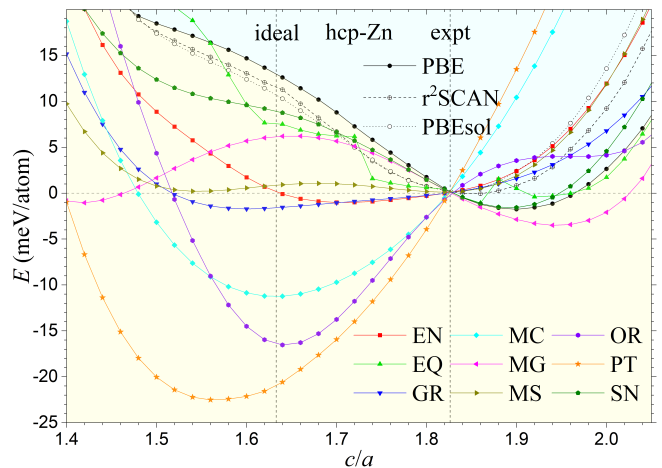


FIG. 4. DFT and MLP energy profiles of hcp-Zn as a function of c/a for fixed-volume unit cells. Each curve is set to zero at the experimental $c/a = 1.826$ ratio.

p hybridization that opens up a density of states (DOS) pseudogap and places it near E_F . The demonstrated synchronized alignment of multiple hybridization gaps from opposite directions suggests that the structural distortion is a manifestation of an electronic topological transition triggered by the varying lattice parameters. To illustrate that this stabilization is tied directly to symmetry-controlled hybridization features at E_F , we compare band structures of hcp- and fcc-Zn in Fig. 3. Representation of both close-packed crystal structures with hexagonal unit cells at the experimental $c/a = 1.826$ ratio extrapolated to zero Kelvin [83] helps appreciate that it is the stacking sequence that determines the band splitting at the L and M k-points, which ultimately leads to the appearance of a pseudogap near E_F , present in hcp-Zn (ABABAB) but absent in fcc-Zn (ABCABC).

We examined the ability of the uMLPs to reproduce the structural anomaly in hcp-Zn by first relaxing the volume with each model and then performing single-point calculations for c/a ratios around 1.826 at the fixed optimal volume. This constraint allowed us to sample the shallow trough on the PES over a wide range of structural parameters with a variation of ~ 20 meV/atom, the energy scale of interest (see Fig. S4). Fig. 4 shows that the three DFT approximations correctly predict the departure from the ideal packing and place the c/a minimum at 1.894 (PBE), 1.826 (PBEsol), and 1.840 (r^2 SCAN), but the uMLPs have difficulty reproducing the reference methods. SN is the only model that closely follows the PBE energy profile. EQ also favors configurations with large c/a ratios but produces ~ 5 -meV/atom jumps along the trajectory; the observed artifact is consistent with the findings of Fu *et al.* [53] who noted that grid-based spherical harmonic projections in EQ and eSCAN can introduce discretization artifacts that degrade both smoothness and energy conservation. EN, GR, and MS are aware of the energy basin’s peculiar shape but do not

properly favor the structural distortion, yielding nearly flat curves with a ~ 2 meV/atom variation between the ideal and the experimental ratios. MC, OR, and PT fail to recognize the stabilizing effect of the distortion and define a pronounced minimum around the ideal c/a . MG agrees with PBE qualitatively, predicting a large c/a optimal ratio, but the feature appears fortuitous because of the presence of a second comparable minimum at unphysically small c/a around 1.42. Our own attempts to accurately reproduce the dependence with a Behler-Parrinello NN potential constructed with our standard protocol [16] failed even after the distorted configurations were heavily weighted in the reference data set and the regularization factor was relaxed, with best versions (not shown) displaying EN-like behavior.

B. Competing MB₄ phases for 3d metals

Ground states of 3d metal tetraborides feature a complex morphology of interlinked B₄ units (Fig. 5). The shape of the 3D B framework and the arrangement of the metal atoms are sensitive to the electron count and remained misidentified in CrB₄ and MnB₄ long after their discovery. In 2010, an *ab initio* evolutionary search for FeB₄ found a new oP10 structure [78],[85], a distorted derivative of the oI10 CrB₄ prototype, to be thermodynamically stable under moderate pressures; the phase was subsequently synthesized at above 8 GPa and quenched to ambient conditions [86]. An *ab initio* reexamination of CrB₄ revealed that the compound also prefers the oP10 polymorph over the originally assigned oI10; the prediction was later confirmed by single-crystal XRD measurements [87],[88]. Similarly, several DFT studies reanalyzed MnB₄ and proposed a lower-symmetry mP20 ground state [80, 89, 90]; the refined solution was verified experimentally as well [89, 90]. The definitive determination of ground states proved essential for this materials family, as FeB₄ and MnB₄ have been shown to superconduct at 2.7 K (1 bar) [86] and 14.2 K (150 GPa) [91], respectively. While all three compounds are non-magnetic, with ferromagnetic order vanishing in the Fe-B binary around the dilute 1:4 metal concentration [80], spin fluctuations appear to play an important role in the pairing interaction, suppressing the conventional T_c in FeB₄ and possibly contributing to the high T_c in MnB₄. Hence, the electronically frustrated MB₄ compounds present a trying test case for the capability of MLPs to resolve competing crystal structures.

As a baseline, we examined how commonly used DFT flavors, PBE, r²SCAN, and PBEsol describe the relative stability of the three configurations. The three approximations correctly predict that CrB₄ and FeB₄ benefit from the oI10→oP10 transformation that skews the B₄ rectangles and that MnB₄ further stabilizes through the oP10→mP20 symmetry breaking that dimerizes Mn atoms along the metal linear chains. Fig. 5 and Table S2 show that the energy gains agree to within 3–5, 8.6, and

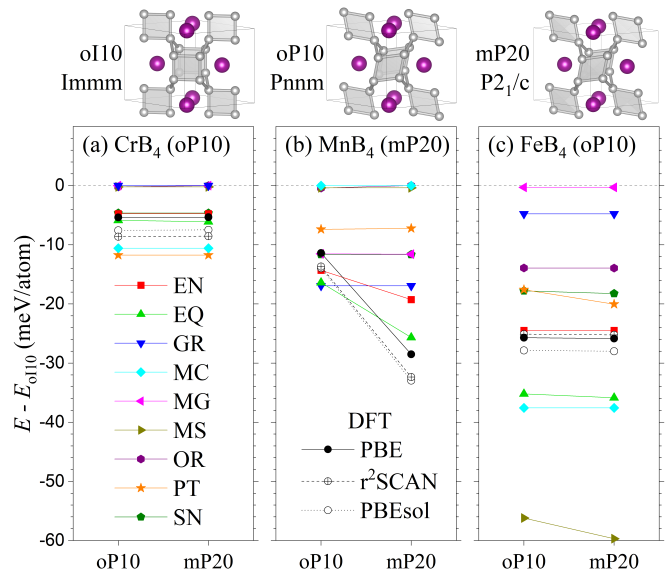


FIG. 5. Stability of distorted oP10 and mP20 derivatives relative to oI10 calculated with DFT and uMLPs for MB₄ with (a) M = Cr, (b) M = Mn, and (c) M = Fe. The oI10 and oP10 structures are displayed with supercells to illustrate the connection with the lowest-symmetry mP20.

8.0 meV/atom for CrB₄, 25.7, 25.1, and 28.4 meV/atom for FeB₄, and 28.5, 32.4, and 33.7 meV/atom for MnB₄, respectively. In CrB₄, the higher stabilization found for r²SCAN and PBEsol reflects the larger level of the B₄ distortion.

Local optimizations of the three prototypes with each uMLP were performed starting from conventional PBE-relaxed unit cells, and Fig. 5 displays the energy of the oP10 and mP20 derivatives relative to the undistorted oI10 structure in each compound. For FeB₄, all uMLPs capture the dynamical instability of the oI10 prototype with respect to the Γ -point B phonon mode which generates oP10 with an unexpected *increase* of the DOS at the Fermi level [78]. However, MG shows no measurable energy gain, GR underestimates the stabilization by a factor of five, MS overestimates it twofold, and PT, SN, and MS favor further monoclinic distortion. The full relaxation of the oP10 prototype reduces the right angle in the B₄ units to about 60° and increases the coordination of half of the B atoms by bringing a neighbor within a near-covalent 1.9 Å bond length in all but the MG parametrization (see Table S2). For CrB₄, EQ, EN, MC, SN, PT, and MS are able to reproduce the slight favorability of the oP10 prototype. For MnB₄, GR, OR, and MG find oI10 to be locally stable, SN, MC, and PT improve it to the oP10 derivative, MS introduces a slight mP20 distortion, and only EN and EQ correctly identify mP20 as the ground state. The two models are in quantitative agreement with PBE, matching the stabilization gain to within 10 meV/atom and the dimerized Mn-Mn nearest distances, which contract from 2.93 Å in oI10 down to 2.65 Å in mP20, to within 1%.

These tests illustrate that some of the examined uMLPs could successfully serve as surrogate models in unconstrained searches to locate the low-symmetry ground states in this materials family. The distorted prototypes would be correctly identified to have the lowest energy at the DFT level with a simple reoptimization of the candidate pool rather than an expensive phonon dispersion analysis. EQ and EN perform best by reproducing the distorted derivatives for all three MB₄ compounds; SN, MC, and PT correctly identify ground states for CrB₄ and FeB₄; GR and OR are able to recognize the favorability of the symmetry breaking only for FeB₄; MS points to oI10 instability across all three MB₄ compounds without clearly preferring any of the correct ground states; and MG predicts a very shallow basin around the oI10 parent structure in this materials family.

C. Off-stoichiometry LiB_y phases

The structure and the composition of LiB_{y<1}, discovered in late 1970s [92], remained a puzzle for decades until an in-depth XRD analysis showed that the compound is comprised of linear B chains and a Li sublattice with incommensurate periods [93]. Subsequent modeling of LiB_y with structures of varying sublattice ratios revealed that their formation energies follow a parabolic dependence on the composition [94], which defines a finite range of stability around the experimentally observed $y = 0.9$ ($x = (1+y)^{-1} = 0.526$). While deviations from ideal stoichiometries are common at elevated temperatures due to the configurational entropy contribution to the formation free energy, the existence of a finite stability range at zero temperature is unique. According to the *ab initio* analysis [94], the Li to B charge transfer does not follow a simple rigid band shift scenario because Li preferentially downshifts $p_{x,y}$ B orbitals, and the resulting DOS pseudogap moves close to the Fermi level at the observed x values. The established parabolic dependence has helped explain the material's response to H₂ exposure [95], track its composition under compression [94], [96], [97], and prime its proposed function as a precursor for synthesis of a layered LiB superconductor [98].

The material is a particularly valuable testbed for uMLPs because the off-stoichiometric ground state phases, not yet added to major materials databases, have not been included in the uMLP training sets. For example, the Materials Project has only one suboptimal representative of the material, α -LiB. Fig. 6 and Table S3 illustrate how we used the Li_{2n}B_m series to probe whether uMLPs are capable of capturing the stability range, with x_{\min} and x_{\max} defined by tangents to the parabolic fits $1/2c(x - x_0)^2 + E_0$ from LiB₃ and Li points on the formation energy plot, respectively.

Our DFT results reflect the known strong dependence of formation energies on the exchange-correlation functional values for α -LiB and LiB₃ disperse by up to 50

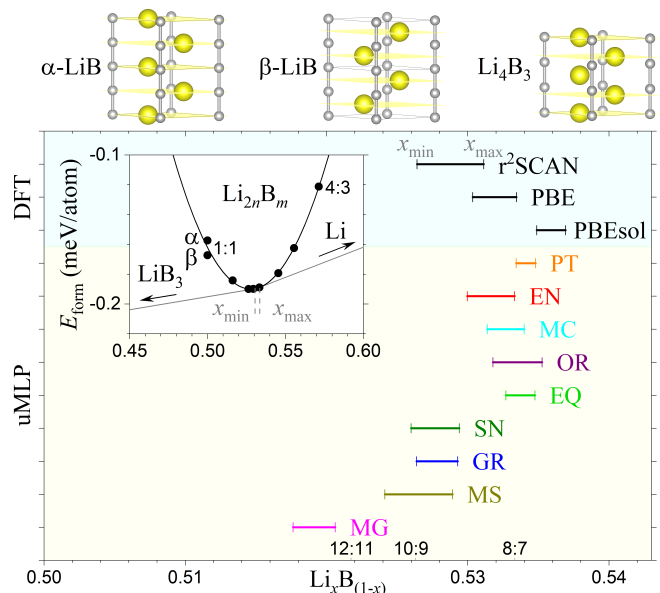


FIG. 6. Stability ranges for Li_xB_{1-x} phases with linear B chains for DFT and MLPs. The inset shows the parabolic fit to the PBE formation energies, with x_{\min} and x_{\max} values determined as parabola tangents connecting LiB₃ and Li, respectively.

meV/atom. For this reason, our uMLP benchmarking focuses primarily on properties that are either intrinsic to the LiB_y family, such as the energy difference between α and β LiB phases with alternative relative placement of the B and Li sublattices, or at least invariant under affine transformations ($E' = E + A + Bx$), such as the fitted parabolic curvature and the ranges of stability (see Supplementary Note I). The three DFT approximations indeed produce closely matching values for $\Delta E_{\alpha\text{-LiB}} = 9.2 - 10.7$ meV/atom and $c = 72 - 75$ eV/atom, but the $[x_{\min}, x_{\max}]$ estimates show a larger dispersion, with PBE and PBEsol defining non-overlapping ranges different by a factor of two (Fig. 6).

The uMLPs correctly favor β over α but the energy difference is noticeably underestimated, especially for MS, SN, and PT. The fitted curvatures are also consistently softer, at 60-85% of the PBE value. The results show that these classical models do not sufficiently penalize the sublattice shifts away from the natural Li-B registry or the compositional deviations from the optimal stoichiometry. At the same time, the PBE stability ranges are reproduced by the uMLPs with accuracy that is better (ES, MC, OR, and EQ) or comparable (SN, GR, and MS) to that of the PBEsol or r²SCAN estimates, while PT is in a reasonable agreement with the PBEsol reference. The fact that all uMLPs place the minimum of the LiB_y formation energy curve in the Li-rich region, in quantitative agreement with the *ab initio* methods, could be an indication that the stable stoichiometries are determined predominantly by classical factors, *e.g.*, the ratio of the effective Li and B sizes [94], and that the redis-

tribution of electronic states is consequential rather than causal.

For assessing the quality of the LiB_y description further away from equilibrium, we also calculated the relative stability between β -LiB and a layered hP8-LiB phase. The latter was predicted to stabilize under pressure [99], and was later synthesized via cold compression and annealed to ambient conditions [97]. The conversion apparently follows a low-barrier pathway linking B chains into honeycomb B layers, a process that requires large-scale simulations to model. uMLPs could therefore shed light on the kinetics of the solid-state transformation, provided that they accurately resolve the relative energy between the hP8-LiB and β -LiB endpoints. In practice, the values vary substantially even across the DFT approximations, with -3.5 meV/atom for PBE, $+26.6$ meV/atom for $r^2\text{SCAN}$, and -32.9 meV/atom for PBEsol, and disperse over a wider range with uMLPs, with -110 meV/atom for MC and $+153$ meV/atom for MG (see Table S3). Among the considered models, only EN, GR, OR, and PT reproduce their respective references closely enough to distinguish reliably between the two competing phases with markedly different morphologies.

V. SUMMARY

This study presents a systematic benchmark of nine state-of-the-art uMLPs through evolutionary crystal structure prediction. Unlike traditional testing frameworks that often rely on libraries of commonly observed high-symmetry structures, our protocol probed the models' readiness for practical unconstrained explorations that have a track record in the accelerated discovery of new thermodynamically stable prototypes [11, 12]. By focusing on multicomponent materials, we evaluated the uMLPs' ability to describe diverse bonding mechanisms and complex ground states. The inclusion of three compounds with recently proposed ground states, Li_3Sn , Pd_5Sn_3 , and MgB_3C_3 , further tested whether out-of-the-box uMLPs can handle configurations absent from their training sets.

The results reveal an impressive level of predictive maturity across the latest generation of models. With the exception of the earliest architecture, the considered uMLPs successfully managed unconstrained searches, locating ground states for most compounds (see Table II and Fig. 2). The remarkably low rate of unphysical artifacts indicates that current training sets provide a robust baseline for inorganic chemistry. AgClO_4 was the sole compound where all models struggled due to insufficient sampling of specific oxygen bonding environments.

Our combined qualitative and quantitative analysis shown in Table II and Fig. 2 and summarized in Table III allows for a more contextual understanding of model behavior that simple accuracy metrics cannot capture alone. The specific success rates should be interpreted

cautiously because evolutionary exploration is stochastic, but the accumulated data set, comprising over two million uMLP local relaxations and more than seven thousand DFT calculations, is large enough to make these trends identifiable. For example, EQ has the second-lowest ranking RMSE, yet its evolutionary searches generated considerably larger pools of low-symmetry candidate structures, suggesting that not reaching the ground states for two compounds was not accidental. At the other end of the accuracy spectrum, MG exhibits RMSE values typical of smaller uMLPs and within the DFT systematic spread, but proved singularly ineffective in nearly all unconstrained runs.

Rather unexpectedly, the extensive structure searches carried out purely for benchmarking purposes identified two phases lying below the previously reported global minima at the reference DFT level. The tI10- Na_2CN_2 candidate is favored only with PBE, making it a likely functional-specific artifact. The oI28- MgB_3C_3 phase ranks below the proposed layered superconducting polymorph [41] across all considered exchange-correlation functionals, indicating that deintercalation of the MgB_2C_2 precursor may lead to products with morphologies unrelated to the starting honeycomb framework.

We also examined whether current uMLPs can map subtle near-equilibrium PES features arising from electronic structure peculiarities. As in our multi-metric evaluation of global optimization performance, we assigned composite qualitative and quantitative scores to assess reproduction of the relevant observables described in the caption of Table III. In this case, we focused on prospective simulations probing structural response and phase transformations on scales for which direct DFT validation may be prohibitively expensive.

For the well-studied hcp-Zn, most uMLPs struggled to reproduce the shallow basin around the anomalous c/a ratio defined by the electronic band topology [82]. Only SN closely follows the reference energy profile and could be used in molecular dynamics simulations to model, in particular, the observed c/a response to temperature [83]. For the CrB_4 , FeB_4 , and MnB_4 compounds, several uMLPs correctly reproduce the chemistry-dependent symmetry lowering among the competing oI10, oP10, and mP20 polymorphs. The performance is encouraging for future large-scale exploration of the $(\text{Cr,Mn,Fe})\text{B}_4$ phase space aimed at identifying synthesizable superconducting and superhard materials without exhaustive *ab initio* stability analyses for every distortion pattern [78, 80, 85]. For off-stoichiometric LiB_y , all uMLPs correctly place the stability minimum in the Li-rich region near $y \approx 0.9$, despite standard databases still listing LiB as the ground-state composition. Detailed modeling of the experimentally observed structural transformation from the ambient-pressure precursor to a layered phase with potential for high- T_c superconductivity [97, 98] demands accurate description of the competing Li-B phases. While several uMLPs agree

TABLE III. Aggregate performance of the considered uMLPs, classified by fitted-parameter count listed in Table I, with respect to their reference DFT method. Details of the global search success rates for 12 inorganic compounds are presented in Table II, while accuracy metrics averaged over the identified pools of low-energy candidates are shown in Fig. 2. Description quality of near-equilibrium configurations for selected compounds is assessed with a composite score on a 12-point scale. For hcp-Zn, the evaluation criteria are the location of the global minimum at the anomalous c/a ratio, PES smoothness, and absence of pronounced secondary minima (Fig. 4). For the MB_4 family, the grades reflect the qualitative identification of the ground-state polymorph (mP20 for Mn and oP10 for Cr and Fe) and the quantitative agreement, within 10 meV/atom, of the distortion-driven stabilization (Fig. 5 and Table S3). For LiB_y , the scores indicate the favorability of Li-rich phases ($y \approx 0.9$) and reproduction of the relative stabilities among relevant LiB phases (Fig. 6 and Table S3).

uMLP			Global search	Pool metrics			Ground state perturbations		
Name	ID	Size	Success rate	RMSE	Prox(E)	Prox(S)	hcp-Zn	MB_4	LiB_y
eSEN	EN	Medium	11 (92%)	5.28	0.44	0.75	8	12	11
SevenNet	SN	Medium	11 (92%)	11.23	2.60	0.61	12	12	6
GRACE	GR	Medium	11 (92%)	11.42	2.40	0.62	8	4	12
Orb-v3	OR	Medium	10 (83%)	10.22	2.37	0.66	2	6	11
EquiformerV2	EQ	Large	9 (75%)	6.94	1.89	0.66	10	12	7
PET-MAD	PT	Small	9 (75%)	16.26	7.23	0.49	4	12	10
MACE	MC	Medium	10 (83%)	19.79	5.34	0.54	4	6	9
MatterSim	MS	Small	8 (67%)	23.67	7.96	0.56	6	0	6
M3GNet	MG	Small	2 (17%)	23.97	70.29	0.42	0	4	6

with the reference method, the common semi-local DFT approximations themselves do not account for the vdW interactions important in this materials class.

Overall, the benchmark indicates that current pre-trained uMLPs can already boost *ab initio* global optimization and accurately describe selected near-equilibrium PES features, with EN delivering the most consistent performance across the tested cases. The results are consistent with the general trend that larger models with more expressive descriptors and broader training coverage transfer more reliably across competing structures and chemistries. In this respect, system-specific potentials may no longer need to be the default starting point for crystal structure exploration. Any application to a specific materials problem should still be preceded by case-specific validation and, when needed, retraining against an appropriate reference set. This caution is especially important because no exchange-correlation approximation is universally accurate across the periodic table.

CONFLICTS OF INTEREST

There are no conflicts to declare.

DATA AVAILABILITY

The data supporting the findings of this study are available within the article and its supplementary information file. Additional data are available from the corresponding author upon request.

ACKNOWLEDGMENTS

The authors thank Aidan Thorn and Erin Delargy for their help with constructing neural network potentials for Zn and acknowledge support from the National Science Foundation (NSF) (Award No. DMR-2320073). This work used the Expanse system at the San Diego Supercomputer Center via allocation TG-DMR180071. Expanse is supported by the Extreme Science and Engineering Discovery Environment (XSEDE) program [100] through NSF Award No. ACI-1548562. The work of O.G. was supported by SCALE (Scalable Asymmetric Lifecycle Engagement).

-
- [1] J. Behler and M. Parrinello, Generalized neural-network representation of high-dimensional potential-energy surfaces, *Phys. Rev. Lett.* **98**, 146401 (2007).
- [2] A. P. Bartók, M. C. Payne, R. Kondor, and G. Csányi, Gaussian approximation potentials: The accuracy of quantum mechanics, without the electrons, *Phys. Rev. Lett.* **104**, 136403 (2010).
- [3] V. L. Deringer, M. A. Caro, and G. Csányi, Machine learning interatomic potentials as emerging tools for materials science, *Adv. Mater.* **31**, 1902765 (2019).
- [4] G. L. W. Hart, T. Mueller, C. Toher, and S. Curtarolo, Machine learning for alloys, *Nat. Rev. Mater.* **6**, 730 (2021).

- [5] Y. Mishin, Machine-learning interatomic potentials for materials science, *Acta Materialia* **214**, 116980 (2021).
- [6] S.-D. Huang, C. Shang, P.-L. Kang, and Z.-P. Liu, Atomic structure of boron resolved using machine learning and global sampling, *Chem. Sci.* **9**, 8644 (2018).
- [7] E. V. Podryabinkin, E. V. Tikhonov, A. V. Shapeev, and A. R. Oganov, Accelerating crystal structure prediction by machine-learning interatomic potentials with active learning, *Phys. Rev. B* **99**, 064114 (2019).
- [8] J. Behler, R. Martoňák, D. Donadio, and M. Parrinello, Metadynamics simulations of the high-pressure phases of silicon employing a high-dimensional neural network potential, *Phys. Rev. Lett.* **100**, 185501 (2008).
- [9] V. L. Deringer, D. M. Proserpio, G. Csányi, and C. J. Pickard, Data-driven learning and prediction of inorganic crystal structures, *Faraday Discuss.* **211**, 45 (2018).
- [10] W. Ibarra-Hernández, S. Hajinazar, G. Avendaño-Franco, A. Bautista-Hernández, A. N. Kolmogorov, and A. H. Romero, Structural search for stable Mg–Ca alloys accelerated with a neural network interatomic model, *Phys. Chem. Chem. Phys.* **20**, 27545 (2018).
- [11] S. Kharabadze, A. Thorn, E. A. Koulakova, and A. N. Kolmogorov, Prediction of stable Li–Sn compounds: boosting ab initio searches with neural network potentials, *npj Comput. Mater.* **8**, 136 (2022).
- [12] A. Thorn, D. Gochitashvili, S. Kharabadze, and A. N. Kolmogorov, Machine learning search for stable binary Sn alloys with Na, Ca, Cu, Pd, and Ag, *Phys. Chem. Chem. Phys.* **25**, 22415 (2023).
- [13] R. Ouyang, Y. Xie, and D.-e. Jiang, Global minimization of gold clusters by combining neural network potentials and the basin-hopping method, *Nanoscale* **7**, 14817–14821 (2015).
- [14] K. Gubaev, E. V. Podryabinkin, G. L. W. Hart, and A. V. Shapeev, Accelerating high-throughput searches for new alloys with active learning of interatomic potentials, *Comput. Mater. Sci.* **156**, 148 (2019).
- [15] S. Hajinazar, J. Shao, and A. N. Kolmogorov, Stratified construction of neural network based interatomic models for multicomponent materials, *Phys. Rev. B* **95**, 014114 (2017).
- [16] S. Hajinazar, A. Thorn, E. D. Sandoval, S. Kharabadze, and A. N. Kolmogorov, MAISE: Construction of neural network interatomic models and evolutionary structure optimization, *Comput. Phys. Commun.* **259**, 107679 (2021).
- [17] P. E. Dolgirev, I. A. Kruglov, and A. R. Oganov, Machine learning scheme for fast extraction of chemically interpretable interatomic potentials, *AIP Adv.* **6**, 085318 (2016).
- [18] N. Artrith, T. Morawietz, and J. Behler, High-dimensional neural-network potentials for multicomponent systems: Applications to zinc oxide, *Phys. Rev. B* **83**, 153101 (2011).
- [19] C. J. Pickard, Ephemeral data derived potentials for random structure search, *Phys. Rev. B* **106**, 014102 (2022).
- [20] C. Chen and S. P. Ong, A universal graph deep learning interatomic potential for the periodic table, *Nat. Comput. Sci.* **2**, 718 (2022).
- [21] B. Póta, P. Ahlawat, G. Csányi, and M. Simoncelli, Thermal conductivity predictions with foundation atomistic models, arXiv:2408.00755 (2024), arXiv:2408.00755 [cond-mat.mtrl-sci].
- [22] K. Sharma, A. Loew, H. Wang, F. A. Nilsson, M. Jain, M. A. L. Marques, and K. S. Thygesen, Accelerating point defect photo-emission calculations with machine learning interatomic potentials, *npj Comput. Mater.* **11**, 18201 (2025).
- [23] H. Yu, M. Giantomassi, G. Materzanini, J. Wang, and G.-M. Rignanese, Systematic assessment of various universal machine-learning interatomic potentials, *Mater. Genome Eng. Adv.* **2**, e58 (2024).
- [24] A. Loew, D. Sun, H.-C. Wang, S. Botti, and M. A. L. Marques, Universal machine learning interatomic potentials are ready for phonons, *npj Comput. Mater.* **11**, 10 (2025).
- [25] J. Riebesell, R. E. A. Goodall, P. Benner, Y. Chiang, B. Deng, G. Ceder, M. Asta, A. A. Lee, A. Jain, and K. A. Persson, A framework to evaluate machine learning crystal stability predictions, *Nat. Mach. Intell.* **7**, 836 (2025).
- [26] Y. Chiang, T. Kreiman, C. Zhang, M. C. Kuner, E. Weaver, I. Amin, H. Park, Y. Lim, J. Kim, D. Chrzan, A. Walsh, S. M. Blau, M. Asta, and A. S. Krishnapriyan, MLIP Arena: Advancing Fairness and Transparency in Machine Learning Interatomic Potentials via an Open, Accessible Benchmark Platform, arXiv preprint arXiv:2509.20630 10.48550/arXiv.2509.20630 (2025).
- [27] H. Tahmasbi, A. Knüpfer, T. D. Kühne, and H. Mirhosseini, Benchmarking Universal Machine Learning Interatomic Potentials on Elemental Systems, arXiv preprint arXiv:2512.20230 10.48550/arXiv.2512.20230 (2025).
- [28] A. Peng, C. Cai, M. Guo, D. Zhang, C. Zhang, W. Jiang, Y. Wang, A. Loew, C. Wu, W. E. L. Zhang, and H. Wang, Lambench: a benchmark for large atomistic models, *npj Computat. Mater.* **12**, 62 (2026).
- [29] A. Loew, J. Schmidt, S. Botti, and M. A. L. Marques, Universal machine learning potentials under pressure, *Journal of Physics: Materials* **9**, 015010 (2025).
- [30] P. Lyngby, C. Larsen, and K. W. Jacobsen, Bayesian optimization of atomic structures with prior probabilities from universal interatomic potentials, *Phys. Rev. M* **8** (2024).
- [31] G. Mair, H.-G. von Schnering, M. Wörle, and R. Nesper, Dilithium Hexaboride, Li_2B_6 , *Z. Anorg. Allg. Chem.* **625**, 1207 (1999).
- [32] D.-H. Wang, H.-Y. Zhou, C.-H. Hu, Y. Zhong, A. R. Oganov, and G.-H. Rao, Prediction of thermodynamically stable Li–B compounds at ambient pressure, *Phys. Chem. Chem. Phys.* **19**, 8471 (2017).
- [33] S. K. Choi, R. Coldea, A. N. Kolmogorov, T. Lancaster, I. I. Mazin, S. J. Blundell, P. G. Radaelli, Y. Singh, P. Gegenwart, K. R. Choi, S.-W. Cheong, P. J. Baker, C. Stock, and J. Taylor, Spin Waves and Revised Crystal Structure of Honeycomb Iridate Na_2IrO_3 , *Phys. Rev. Lett.* **108**, 127204 (2012).
- [34] H. J. Becher and A. Schäfer, Darstellung und Struktur des Berylliumborids Be_4B , *Z. Anorg. Allg. Chem.* **318**, 304 (1962).
- [35] A. Hermann, N. W. Ashcroft, and R. Hoffmann, Binary compounds of boron and beryllium: A rich structural arena with space for predictions, *Chemistry – A European Journal* **19**, 4184 (2013).
- [36] C. J. Howard, T. M. Sabine, and F. Dickson, Structural and thermal parameters for rutile and anatase, *Acta*

- Crystallogr. Sect. B: Struct. Sci. **47**, 462 (1991).
- [37] G. Eguchi, D. C. Peets, M. Kriener, Y. Maeno, E. Nishibori, Y. Kumazawa, K. Banno, S. Maki, and H. Sawa, Crystallographic and superconducting properties of the fully gapped noncentrosymmetric 5d-electron superconductors CaMSi_3 ($M = \text{Ir, Pt}$), Phys. Rev. B **83**, 024512 (2011).
- [38] K.-H. Ahn, H.-J. Lee, D. Johrendt, and K. A. Müller, Influence of pressure on the structure and electronic properties of the layered superconductor $\text{Y}_2\text{C}_2\text{I}_2$, J. Phys. Condens. Matter **17**, L637 (2005).
- [39] D. Errandonea, L. Gracia, A. Beltrán, A. Vegas, and Y. Meng, Pressure-induced phase transitions in AgClO_4 , Phys. Rev. B **84**, 064103 (2011).
- [40] Y. Zhang, J. W. Furness, B. Xiao, and J. Sun, Subtlety of TiO_2 phase stability: Reliability of the density functional theory predictions and persistence of the self-interaction error, J. Chem. Phys. **150**, 014105 (2019).
- [41] C. R. Tomassetti, D. Gochitashvili, C. Renskers, E. R. Margine, and A. N. Kolmogorov, First-principles design of ambient-pressure $\text{Mg}_x\text{B}_2\text{C}_2$ and Na_xBC superconductors, Phys. Rev. Mater. **8**, 114801 (2024).
- [42] I. Batatia, D. P. Kovács, G. N. C. Simm, C. Ortner, and G. Csányi, MACE: Higher Order Equivariant Message Passing Neural Networks for Fast and Accurate Force Fields, in *Adv. Neural Inf. Process. Syst. (NeurIPS)*, Vol. 35 (2022) pp. 11423–11436.
- [43] I. Batatia, S. Batzner, D. P. Kovács, A. Musaelian, G. N. C. Simm, R. Drautz, C. Ortner, B. Kozinsky, and G. Csányi, The design space of E(3)-equivariant atom-centred interatomic potentials, Nature Machine Intelligence **7**, 56–67 (2025).
- [44] Y. Park, J. Kim, S. Hwang, and S. Han, Scalable parallel algorithm for graph neural network interatomic potentials in molecular dynamics simulations, J. Chem. Theory Comput. **20**, 4857 (2024).
- [45] J. Kim, J. Kim, J. Kim, J. Lee, Y. Park, Y. Kang, and S. Han, Data-Efficient Multifidelity Training for High-Fidelity Machine Learning Interatomic Potentials, J. Am. Chem. Soc. **147**, 1042 (2024).
- [46] Y.-L. Liao, B. Wood, A. Das, and T. Smidt, EquiformerV2: Improved Equivariant Transformer for Scaling to Higher-Degree Representations, in *International Conference on Learning Representations (ICLR)* (2024).
- [47] L. Barroso-Luque, M. Shuaibi, X. Fu, B. M. Wood, M. Dzamba, M. Gao, A. Rizvi, C. L. Zitnick, and Z. W. Ulissi, Open Materials 2024 (OMat24) Inorganic Materials Dataset and Models, arXiv preprint arXiv:2410.12771 10.48550/arXiv.2410.12771 (2024).
- [48] Y.-L. Liao and T. Smidt, Equiformer: Equivariant Graph Attention Transformer for 3D Atomistic Graphs, in *International Conference on Learning Representations (ICLR)* (2023).
- [49] L. Chanussot, A. Das, S. Goyal, T. Lavril, M. Shuaibi, M. Riviere, K. Tran, J. Heras-Domingo, C. Ho, W. Hu, A. Palizhati, A. Sriram, B. Wood, J. Yoon, D. Parikh, C. L. Zitnick, and Z. Ulissi, Open Catalyst 2020 (OC20) Dataset and Community Challenges, ACS Catal. **11**, 6059 (2021).
- [50] H. Yang, C. Hu, Y. Zhou, X. Liu, Y. Shi, J. Li, G. Li, Z. Chen, S. Chen, C. Zeni, M. Horton, R. Pinsler, A. Fowler, D. Zügner, T. Xie, J. Smith, L. Sun, Q. Wang, L. Kong, C. Liu, H. Hao, and Z. Lu, Mat-terSim: A Deep Learning Atomistic Model Across Elements, Temperatures and Pressures, arXiv preprint arXiv:2405.04967 10.48550/arXiv.2405.04967 (2024).
- [51] A. Bochkarev, Y. Lysogorskiy, and R. Drautz, Graph atomic cluster expansion for semilocal interactions beyond equivariant message passing, Phys. Rev. X **14**, 021036 (2024).
- [52] Y. Lysogorskiy, A. Bochkarev, and R. Drautz, Graph atomic cluster expansion for foundational machine learning interatomic potentials, arXiv preprint arXiv:2508.17936 10.48550/arXiv.2508.17936 (2025).
- [53] X. Fu, B. M. Wood, L. Barroso-Luque, D. S. Levine, M. Gao, M. Dzamba, and C. L. Zitnick, Learning Smooth and Expressive Interatomic Potentials for Physical Property Prediction, arXiv preprint arXiv:2502.12147 10.48550/arXiv.2502.12147 (2025).
- [54] B. Rhodes, S. Vandenhoute, V. Šimkus, J. Gin, J. Godwin, T. Duignan, and M. Neumann, Orb-v3: atomistic simulation at scale, arXiv preprint arXiv:2504.06231 10.48550/arXiv.2504.06231 (2025).
- [55] M. Neumann, J. Gin, B. Rhodes, S. Bennett, Z. Li, H. Choubisa, A. Hussey, and J. Godwin, Orb: A Fast, Scalable Neural Network Potential, arXiv preprint arXiv:2410.22570 10.48550/arXiv.2410.22570 (2024).
- [56] A. Mazitov, F. Bigi, M. Kellner, P. Pegolo, D. Tisi, G. Fraux, S. Pozdnyakov, P. Loche, and M. Ceriotti, PET-MAD as a lightweight universal interatomic potential for advanced materials modeling, Nat. Commun. **16**, 65662 (2025).
- [57] J. P. Perdew, K. Burke, and M. Ernzerhof, Generalized Gradient Approximation Made Simple, Phys. Rev. Lett. **77**, 3865 (1996).
- [58] J. P. Perdew, A. Ruzsinszky, G. I. Csonka, O. A. Vydrov, G. E. Scuseria, L. A. Constantin, X. Zhou, and K. Burke, Restoring the density-gradient expansion for exchange in solids and surfaces, Phys. Rev. Lett. **100**, 136406 (2008).
- [59] J. W. Furness, A. D. Kaplan, J. Ning, J. P. Perdew, and J. Sun, Accurate and numerically efficient $r^2\text{SCAN}$ meta-generalized gradient approximation, J. Phys. Chem. Lett. **11**, 8208 (2020).
- [60] G. Kresse and J. Hafner, Ab initio molecular dynamics for liquid metals, Phys. Rev. B **47**, 558 (1993).
- [61] G. Kresse and J. Hafner, Ab initio molecular-dynamics simulation of the liquid-metal–amorphous-semiconductor transition in germanium, Phys. Rev. B **49**, 14251 (1994).
- [62] G. Kresse and J. Furthmüller, Efficient iterative schemes for *ab initio* total-energy calculations using a plane-wave basis set, Phys. Rev. B **54**, 11169 (1996).
- [63] G. Kresse and J. Furthmüller, Efficiency of ab-initio total energy calculations for metals and semiconductors using a plane-wave basis set, Comput. Mater. Sci. **6**, 15 (1996).
- [64] P. E. Blöchl, Projector augmented-wave method, Phys. Rev. B **50**, 17953 (1994).
- [65] H. J. Monkhorst and J. D. Pack, Special points for Brillouin-zone integrations, Phys. Rev. B **13**, 5188 (1976).
- [66] P. E. Blöchl, O. Jepsen, and O. K. Andersen, Improved tetrahedron method for Brillouin-zone integrations, Phys. Rev. B **49**, 16223 (1994).
- [67] D. C. Langreth and M. J. Mehl, Beyond the local-density approximation in calculations of ground-state

- electronic properties, *Phys. Rev. B* **28**, 1809 (1983).
- [68] A. Jain, S. P. Ong, G. Hautier, W. Chen, W. D. Richards, S. Dacek, S. Cholia, D. Gunter, D. Skinner, G. Ceder, and K. A. Persson, Commentary: The Materials Project: A materials genome approach to accelerating materials innovation, *APL Mater.* **1**, 011002 (2013).
- [69] J. Klimeš, D. R. Bowler, and A. Michaelides, Chemical accuracy for the van der Waals density functional, *J. Phys.: Condens. Matter* **22**, 022201 (2009).
- [70] J. Klimeš, D. R. Bowler, and A. Michaelides, Van der Waals density functionals applied to solids, *Phys. Rev. B* **83**, 195131 (2011).
- [71] J. Ning, M. Kothakonda, J. W. Furness, A. D. Kaplan, S. Ehlert, J. G. Brandenburg, J. P. Perdew, and J. Sun, Workhorse minimally empirical dispersion-corrected density functional with tests for weakly bound systems: r^2 SCAN + rVV10, *Phys. Rev. B* **106**, 075422 (2022).
- [72] D. Chakraborty, K. Berland, and T. Thonhauser, Next-Generation Nonlocal van der Waals Density Functional, *J. Chem. Theory Comput.* **16**, 5893 (2020).
- [73] S. Batzner, A. Musaelian, L. Sun, M. Geiger, J. P. Mailoa, M. Kornbluth, N. Molinari, T. E. Smidt, and B. Kozinsky, E(3)-equivariant graph neural networks for data-efficient and accurate interatomic potentials, *Nat. Commun.* **13**, 2453 (2022).
- [74] S. Passaro and C. L. Zitnick, Reducing SO(3) Convolutions to SO(2) for Efficient Equivariant GNNs, in *Proc. Mach. Learn. Res. (PMLR)*, Vol. 202 (PMLR, 2023) pp. 27424–27438.
- [75] T. W. Ko, B. Deng, M. Nassar, L. Barroso-Luque, R. Liu, J. Qi, A. C. Thakur, A. R. Mishra, E. Liu, G. Ceder, S. Miret, and S. P. Ong, Materials Graph Library (MatGL), an open-source graph deep learning library for materials science and chemistry, *npj Comput. Mater.* **11**, 253 (2025).
- [76] A. H. Larsen, J. J. Mortensen, J. Blomqvist, I. E. Castelli, R. Christensen, M. Dułak, J. Friis, M. Groves, B. Hammer, C. Hargus, E. Hermes, P. C. Jennings, P. B. Jensen, J. Kermode, J. R. Kitchin, E. Kolsbjerg, J. Kubal, K. Kaasbjerg, S. Lysgaard, J. B. Maronsson, T. Maxson, T. Olsen, L. Pastewka, A. T. Peterson, C. Rostgaard, J. Schiøtz, O. Schütt, M. Strange, K. S. Thygesen, T. Vegge, L. Vilhelmsen, M. Walter, Z. Zeng, and K. W. Jacobsen, The Atomic Simulation Environment — A Python library for working with atoms, *J. Phys. Condens. Matter* **29**, 273002 (2017).
- [77] A. Thorn, J. Rojas-Nunez, S. Hajinazar, S. E. Baltazar, and A. N. Kolmogorov, Toward ab Initio Ground States of Gold Clusters via Neural Network Modeling, *J. Phys. Chem. C* **123**, 30088 (2019).
- [78] A. N. Kolmogorov, S. Shah, E. R. Margine, *et al.*, New Superconducting and Semiconducting Fe-B Compounds Predicted with an Ab Initio Evolutionary Search, *Phys. Rev. Lett.* **105**, 217003 (2010).
- [79] D. Gochitashvili, M. Meyers, C. Wang, and A. N. Kolmogorov, Improving structure search with hyperspatial optimization and TETRIS seeding, *Phys. Chem. Chem. Phys.* **27**, 25636 (2025).
- [80] A. Van Der Geest and A. Kolmogorov, Stability of 41 metal–boron systems at 0GPa and 30GPa from first principles, *Calphad* **46**, 184 (2014).
- [81] T.-T. Pham and D.-L. Nguyen, First-principles prediction of superconductivity in MgB_3C_3 , *Phys. Rev. B* **107**, 134502 (2023).
- [82] U. Häussermann and S. Simak, Origin of the c/a variation in hexagonal close-packed divalent metals, *Phys. Rev. B* **64**, 245114 (2001).
- [83] U. Wedig, H. Nuss, J. Nuss, M. Jansen, D. Andrae, B. Paulus, A. Kirfel, and W. Weyrich, Electronic origin of the structural anomalies of zinc and cadmium, *Z. Anorg. Allg. Chem.* **639**, 2036 (2013).
- [84] K. Takemura, The zinc story under high pressure, *J. Miner. Mater. Charact. Eng.* **7**, 354 (2019).
- [85] A. F. Bialon, T. Hammerschmidt, R. Drautz, *et al.*, Possible routes for synthesis of new boron-rich Fe–B and $\text{Fe}_{1-x}\text{Cr}_x\text{B}_4$ compounds, *Appl. Phys. Lett.* **98**, 081901 (2011).
- [86] H. Gou, N. Dubrovinskaia, E. Bykova, A. A. Tsirlin, D. Kasinathan, A. Richter, M. Merlini, M. Hanfland, A. M. Abakumov, D. Batuk, and L. Dubrovinsky, Discovery of a superhard iron tetraboride superconductor, *Phys. Rev. Lett.* **111**, 157002 (2013).
- [87] H. Niu, J. Wang, X.-Q. Chen, D. Li, Y. Li, P. Lazar, R. Podloucky, and A. N. Kolmogorov, Structure, bonding, and possible superhardness of CrB_4 , *Physical Review B* **85**, 144116 (2012).
- [88] A. Knappschneider, C. Litterscheid, D. Dzivenko, J. A. Kurzman, R. Seshadri, N. Wagner, J. Beck, R. Riedel, and B. Albert, Possible superhardness of CrB_4 , *Inorg. Chem.* **52**, 540 (2013).
- [89] A. Knappschneider, C. Litterscheid, N. C. George, J. Brgoch, N. Wagner, J. Beck, J. A. Kurzman, R. Seshadri, and B. Albert, Peierls-distorted monoclinic MnB_4 with a Mn–Mn bond, *Angew. Chem. Int. Ed.* **53**, 1684 (2014).
- [90] H. Gou, A. A. Tsirlin, E. Bykova, A. M. Abakumov, G. Van Tendeloo, A. Richter, S. V. Ovsyannikov, A. V. Kurnosov, D. M. Trots, Z. Konôpková, and L. Dubrovinsky, Peierls distortion, magnetism, and high hardness of manganese tetraboride, *Phys. Rev. B* **83**, 064108 (2014).
- [91] Z. Xiang, Y. Zhang, Q. Lu, Q. Li, Y. Li, T. Huang, Y. Zhu, Y. Ye, J. Sun, and H. Wen, Superconductivity up to 14.2 k in MnB_4 under pressure, *Advanced Materials* **37** (2024).
- [92] F. E. Wang, M. A. Mitchell, R. A. Sutula, J. R. Holden, and L. H. Bennett, Crystal structure study of a new compound Li_5B_4 , *J. Less-Common Met.* **61**, 237 (1978).
- [93] M. Wörle and R. Nesper, Infinite, linear, unbranched borynide chains in LiB_x —Isoelectronic to polyene and polycumulene, *Angew. Chem.* **112**, 2439 (2000).
- [94] A. N. Kolmogorov and S. Curtarolo, Theoretical study of metal borides stability, *Phys. Rev. B* **74**, 224507 (2006).
- [95] A. N. Kolmogorov, R. Drautz, and D. G. Pettifor, Ab initio modeling of Li–B–H boron-chain alloys for hydrogen storage applications, *Phys. Rev. B* **76**, 184102 (2007).
- [96] A. Hermann, A. Suarez-Alcubilla, I. G. Gurtubay, L.-M. Yang, A. Bergara, N. W. Ashcroft, and R. Hoffmann, LiB and its boron-deficient variants under pressure, *Phys. Rev. B* **86**, 144110 (2012).
- [97] A. N. Kolmogorov, S. Hajinazar, C. Angyal, V. L. Kuznetsov, and A. P. Jephcoat, Synthesis of a predicted layered LiB via cold compression, *Phys. Rev. B* **92**, 144110 (2015).

- [98] G. P. Kafle, C. R. Tomassetti, I. I. Mazin, A. N. Kolmogorov, and E. R. Margine, Ab initio study of Li-Mg-B superconductors, *Phys. R. M* **6**, 084801 (2022).
- [99] A. N. Kolmogorov and S. Curtarolo, Prediction of different crystal structure phases in metal borides: A lithium monoboride analog to MgB_2 , *Phys. Rev. B* **73**, 180501 (2006).
- [100] J. Towns, T. Cockerill, M. Dahan, I. Foster, K. Gaither, A. Grimshaw, V. Hazlewood, S. Lathrop, D. Lifka, G. D. Peterson, R. Roskies, J. R. Scott, and N. Wilkins-Diehr, XSEDE: Accelerating scientific discovery, *Comput. Sci. & Eng.* **16**, 62 (2014).